Multiple harmonic ULF waves in the plasma sheet boundary layer: Instability analysis

R. E. Denton, M. J. Engebretson, A Keiling, A.P. Walsh, S.P. Gary, Pierrette Décréau, Cynthia A. Cattell, H Rème

Multiple harmonic ULF waves in the plasma sheet boundary layer: Instability analysis

R. E. Denton,[1] M. J. Engebretson,[2] A. Keiling,[3] A. P. Walsh,[4] S. P. Gary,[5] P. M. E. Décréau,[6] C. A. Cattell,[7] and H. Rème[8,9]

Received 13 July 2010; revised 7 September 2010; accepted 13 September 2010; published 10 December 2010.

[1] Multiple-harmonic electromagnetic waves in the ULF band have occasionally been observed in Earth's magnetosphere, both near the magnetic equator in the outer plasmasphere and in the plasma sheet boundary layer (PSBL) in Earth's magnetotail. Observations by the Cluster spacecraft of multiple-harmonic electromagnetic waves with fundamental frequency near the local proton cyclotron frequency, Ω_{cp}, were recently reported in the plasma sheet boundary layer by Broughton *et al.* (2008). A companion paper surveys the entire magnetotail passage of Cluster during 2003, and reports 35 such events, all in the PSBL, and all associated with elevated fluxes of counterstreaming ions and electrons. In this study we use observed pitch angle distributions of ions and electrons during a wave event observed by Cluster on 9 September 2003 to perform an instability analysis. We use a semiautomatic procedure for developing model distributions composed of bi-Maxwellian components that minimizes the difference between modeled and observed distribution functions. Analysis of wave instability using the WHAMP electromagnetic plasma wave dispersion code and these model distributions reveals an instability near Ω_{cp} and its harmonics. The observed and model ion distributions exhibit both beam-like and ring-like features which might lead to instability. Further instability analysis with simple beam-like and ring-like model distribution functions indicates that the instability is due to the ring-like feature. Our analysis indicates that this instability persists over an enormous range in the effective ion beta (based on a best fit for the observed distribution function using a single Maxwellian distribution), β', but that the character of the instability changes with β'. For β' of order unity (for instance, the observed case with $\beta' \sim 0.4$), the instability is predominantly electromagnetic; the fluctuating magnetic field has components in both the perpendicular and parallel directions, but the perpendicular fluctuations are larger. If β' is greatly decreased to about 5×10^{-4} (by increasing the magnetic field), the instability becomes electrostatic. On the other hand, if β' is increased (by decreasing the magnetic field), the instability remains electromagnetic, but becomes predominantly compressional (magnetic fluctuations predominantly parallel) at $\beta' \sim 2$. The β' dependence we observe here may connect various waves at harmonics of the proton gyrofrequency found in different regions of space.

Citation: Denton, R. E., M. J. Engebretson, A. Keiling, A. P. Walsh, S. P. Gary, P. M. E. Décréau, C. A. Cattell, and H. Rème (2010), Multiple harmonic ULF waves in the plasma sheet boundary layer: Instability analysis, *J. Geophys. Res.*, *115*, A12224, doi:10.1029/2010JA015928.

1. Introduction

[2] The plasma sheet boundary layer (PSBL) was identified by *Eastman et al.* [1984] and *Parks et al.* [1984] as the temporally variable transition region in the Earth's magnetotail between the relatively dense central plasma sheet and the low-density magnetotail lobes, which are extensions of the Earth's polar cap regions. It is the primary region of

[1]Department of Physics and Astronomy, Dartmouth College, Hanover, New Hampshire, USA.
[2]Department of Physics, Augsburg College, Minneapolis, Minnesota, USA.
[3]Space Sciences Laboratory, University of California, Berkeley, California, USA.
[4]Mullard Space Science Laboratory, University College London, Dorking, UK.
[5]Group ISR-1, Los Alamos National Laboratory, Los Alamos, New Mexico, USA.
[6]LPC2E, UMR 6115, CNRS, Orléans, France.
[7]School of Physics and Astronomy, University of Minnesota, Minneapolis, Minnesota, USA.
[8]CESR, University of Toulouse, UPS, Toulouse, France.
[9]UMR 5187, CNRS, Toulouse, France.

0148-0227/10/2010JA015928

mass, energy, and momentum transport in the magnetotail during quiet times [*Eastman et al.*, 1985], although during more active periods bursty bulk flow events in the central plasma sheet are thought to dominate [*Baumjohann et al.*, 1990; *Angelopoulos et al.*, 1992, 1994]. Observations of the PSBL from a single spacecraft are often of short duration because of the flapping and kink-like motions of the magnetotail that move it in the $\pm Z_{GSE}$ and $\pm Y_{GSE}$ directions, respectively [*Grigorenko et al.*, 2007].

[3] Ion distributions in the PSBL can be summarized as follows: in a broad energy range from ~1 keV/q to >45 keV/q, there is typically a transition from earthward directed beams (i.e., beams with 0° pitch angles in the northern hemisphere and 180° in the southern hemisphere) at the lobe-PSBL boundary, to counterstreaming ion velocity distributions and/or ring-like distributions inside the PSBL, and to nearly isotropic distributions near the central plasma sheet (CPS). Antisunward beams of ionospheric origin (and with energies <1 keV/q) are commonly seen in the lobe and PSBL, but only rarely in the CPS [*Eastman et al.*, 1984]. This progression has led to the suggestion that these two spatially observed transitions are evidence of a temporal process, probably mediated by wave-particle interactions, that can supply hot plasma to the CPS. *Eastman et al.* [1984] also noted that PSBL signatures, including counterstreaming ion flow, occurred at all conditions of geomagnetic activity, including extended quiet periods.

[4] Electron distributions in the PSBL are typically of lower energy than the ions and are often anisotropic (bidirectional and predominantly field-aligned), thus including a beam component that could make them unstable to a variety of electrostatic instabilities, consistent with the simultaneous observation of enhanced simultaneous broadband electrostatic wave activity [*Parks et al.*, 1984].

[5] *Eastman et al.* [1984] identified several possible sources of free energy that were enhanced in the PSBL: (1) significant ion anisotropies with single beams or counterstreaming ion beams which often have positive slopes in the reduced velocity distribution, (2) significant spatial gradients in plasma and field parameters (e.g., ∇n, ∇b, and ∇P), frequently with medium β ($\beta \sim 1$) conditions, and (3) significant field-aligned currents carried primarily by 50–300 eV electrons. Soon after, *Grabbe and Eastman* [1984] presented a theoretical instability analysis suggesting that the energetic ion beams (sunward directed or counterstreaming) were responsible for the broadband electrostatic noise observed in association with those beams. This broadband noise, however, is at frequencies well above those of the waves considered here.

[6] *Janhunen et al.* [2003] investigated the instability of ion shell distributions observed by the Polar satellite at auroral latitudes at ~4–5 R_E radial distance as possible sources of free energy for powering the aurora, and, using the WHAMP code, found that several ion Bernstein modes became unstable under such conditions, and that these waves contribute energy to electrons in the parallel direction. *Olsson et al.* [2004] noted a close association between such shell distributions and simultaneously observed increases in electric wave amplitudes in the 1–10 Hz frequency range, but noted that waves at higher frequencies (10–500 Hz) were also usually excited at the same time. *Olsson et al.* [2004] also noted that the ion shell distributions observed on Polar consisted almost exclusively of H^+ ions. Ion shell distributions with dual loss cones were also noted by *Engebretson et al.* [2002] in Polar satellite data association with electromagnetic ion cyclotron (EMIC) waves observed during very quiet times in the outer dayside magnetosphere.

[7] More recently, *Ashour-Abdalla et al.* [2006] used linear theory to analyze ion shell instabilities in the same altitude range ($R \sim 4$–$5\ R_E$) in the PSBL and found that the shell instability is only excited when a cold ion background is present, and that it excites a broad range of ion cyclotron harmonics. They also used numerical simulations to confirm that ion Bernstein modes are preferentially excited transverse to the magnetic field, and that background electrons are heated symmetrically in the parallel and antiparallel directions.

[8] Waves at multiples of Ω_{cp} have also been observed near Earth's equator in the outer plasmasphere [e.g., *Russell et al.*, 1970; *Perraut et al.*, 1982; *Meredith et al.*, 2008, and references therein], and instabilities responsible for their generation have been similarly addressed. *Perraut et al.* [1982] observed compressional electromagnetic waves (with dominant fluctuations parallel to the background magnetic field) extending from $\omega = \Omega_{cp}$ to the lower hybrid frequency. They found these waves to be associated with ring-like distributions of ions (peaked near 90° pitch angles) with energies between 5 and 30 keV. *Perraut et al.* [1982] identified them as magnetosonic waves, propagating in a direction almost perpendicular to B_0, and suggested that the observed harmonic structure was related to nonlinear effects of locally generated waves rather than the superposition of multiple waves each generated at their local proton gyrofrequency. *Boardsen et al.* [1992] and *Horne et al.* [2000] modeled an instability that could be responsible for these waves using a "subtracted bi-Maxwellian" distribution function (with a population of lower $T_\perp$ subtracted from a population with higher $T_\perp$).

[9] *Liu et al.* [1994], observing similarly structured multiple harmonics of the O^+ gyrofrequency with the EXOS-D satellite at lower L shells, also favored local generation of the multiband emissions. However, *Kokubun et al.* [1991] observed other harmonically related waves at frequencies that were inconsistent with local generation, and inferred inward radial propagation from a higher L shell. Subsequently, *Pokhotelov et al.* [1997] developed a theoretical model suggesting that oscillations at multiple harmonics of the He^+ and O^+ gyrofrequency in the equatorial plasmaphere were also generated by a loss cone or ring-like resonant instability.

[10] *Cattell and Hudson* [1982] examined electrostatic waves at low altitude in the auroral zone, where the plasma beta was very low. These waves were at harmonics of the proton cyclotron frequency near the lower hybrid frequency, and Cattell and Hudson argued that they were driven by a ring-like distribution function.

[11] In this paper we present an analysis of the instability of ion and electron distributions observed in conjunction with multiple harmonics of Ω_{cp} observed by Cluster in the PSBL during one of the events reported by *Engebretson et al.* [2010]. In section 2 we present detailed wave observations, in section 3 we present observed thermal/suprathermal particle distribution functions and results from a semiautomatic procedure for modeling them, and in sections 4 and 5

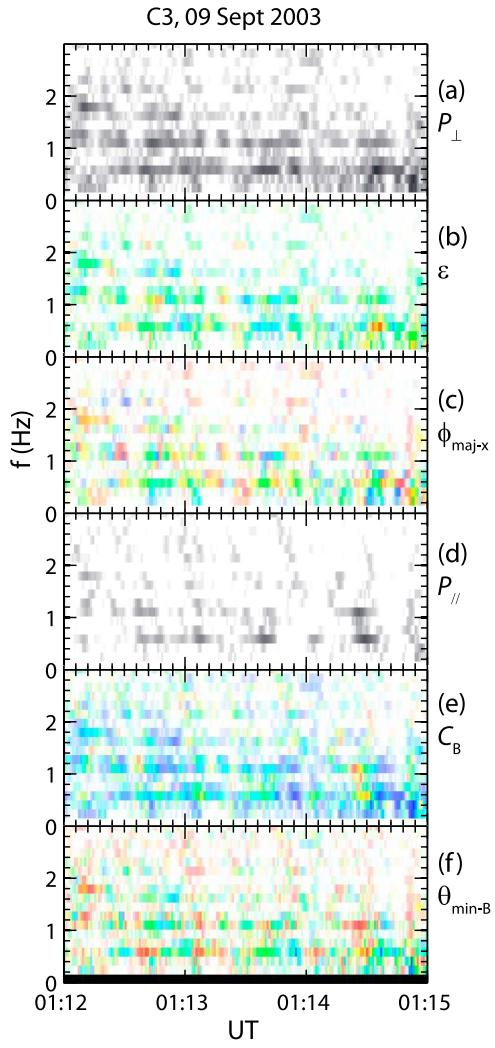

Figure 1. (a) Perpendicular wave magnetic field power $P_\perp$, (b) ellipticity ε, (c) major axis angle to the field aligned x axis $\varphi_{maj\text{-}x}$, (d) parallel wave magnetic field power $P_{||}$, (e) parallel compressibility C_B, and (f) angle between the minimum variance direction and the background magnetic field $\theta_{min\text{-}B}$, all versus UT. (For Figures 1b, 1c, 1e, and 1f, see the two-dimensional color map in Figure 2.)

we present the results of an instability analysis of those modeled distribution functions, using the WHAMP dispersion code. Section 6 follows with some discussion, and conclusions are presented in section 7.

2. Wave Observations

[12] In this paper we focus on one of the two multiple-harmonic ULF wave events presented in detail by *Engebretson et al.* [2010] as part of their survey of all such events during the magnetotail passage of the Cluster orbit from July through October 2003. As shown in Figure 2 of that paper, waves appeared simultaneously at the lowest few harmonics of the proton gyrofrequency Ω_{cp} from ~0104 to 0107 UT and from ~0111 to 0121 UT on 9 September 2003, in close temporal association with increased fluxes of bidirectionally streaming ions and electrons.

[13] Figure 1 shows properties of the waves observed by the FGM instrument [*Balogh et al.*, 2001] on Cluster spacecraft C3 from 0112 to 0115 UT on this day. From top to bottom are the perpendicular wave magnetic field power $P_\perp$ (Figure 1a), the ellipticity ε (Figure 1b), the major axis angle to the field aligned x axis (pointing southward, away from the central plasma sheet) $\varphi_{maj\text{-}x}$ (Figure 1c), the parallel wave magnetic field power $P_{||}$ (Figure 1d), the parallel compressibility C_B (ratio of parallel to total power, Figure 1e), and angle between the minimum variance direction and the background magnetic field $\theta_{min\text{-}B}$ (Figure 1f), all versus UT on the horizontal axis, with frequency on the vertical axis. Data points are plotted at 1 s resolution using a data window for Fourier transform of about 5 s duration (128 data points with time interval 0.0455 s). This time interval is the minimum interval that can resolve the fundamental mode at 0.5 Hz from lower-frequency waves or noise with frequency less than about 0.2 Hz. Within each time window, the linear trend was subtracted, the data was filtered with a Welsh window, and the wave power was moderately whitened by multiplying by the wave frequency (raising the relative power at higher frequencies). The perpendicular (Figure 1a) and parallel (Figure 1d) wave magnetic field power are plotted in gray scale with the same color bar. Therefore it is evident that the perpendicular wave power is larger. The four polarization quantities, ε, $\varphi_{maj\text{-}x}$, C_B, and $\theta_{min\text{-}\mathbf{B}}$ are plotted using the two dimensional color map (color bar) shown in Figure 2. As suggested by Figure 2, blue color corresponds to $\varepsilon = -1$ (left hand polarized waves), $\varphi_{maj\text{-}x} = -90°$ (major axis of perpendicular fluctuations in the field aligned −y direction), $C_B = 0$ (wave power totally perpendicular), and $\theta_{min\text{-}\mathbf{B}} = 0°$ (minimum variance direction field aligned). Looking again at Figures 1b and 1c, we see that ε, $\varphi_{maj\text{-}x}$, and $\theta_{min\text{-}\mathbf{B}}$ vary on a timescale of about 5 s. This suggests that Fourier analysis is not sufficient to examine the polarization and also suggests that there could be superposition of wave packets as described by *Anderson et al.* [1996] and *Denton et al.* [1996]. The results of Denton *et al.* suggest that the ellipticity of superimposed constituent waves is approximately equal to the median value of the observed ellipticity values. Since the observed ellipticity values vary from −1 (left hand polarized)

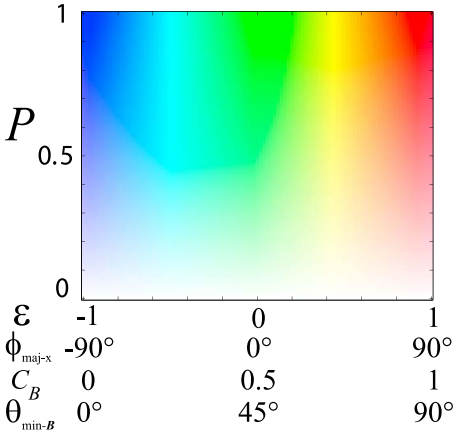

Figure 2. Two-dimensional color map (color bar) with color saturation (darkness) determined by the wave power P (vertical axis) and the hue (color) determined by the quantities listed at the bottom.

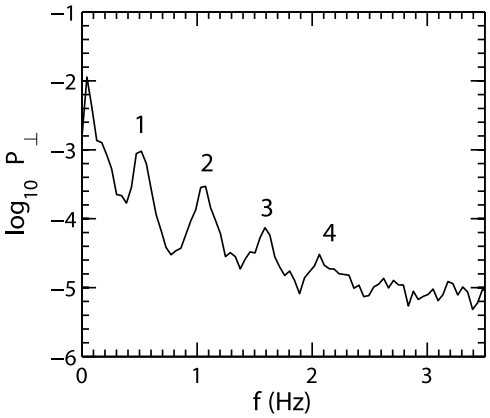

Figure 3. Log average perpendicular wave magnetic field power versus frequency showing the fundamental mode (1) and harmonics (2–4).

to +1 (right hand polarized), this suggests that the ellipticity of the constituent waves might be near zero. For a monochromatic linear wave, $\theta_{\mathbf{min\text{-}B}}$ would be equal to the wave normal angle (angle between the wave vector and the background magnetic field) $\theta_{\mathbf{k\text{-}B}}$. While there appears to be a preference for $\theta_{\mathbf{min\text{-}B}}$ values greater than 45° (preference of red color versus blue color in Figure 1f), this preference is not statistically significant. The power weighted $\theta_{\mathbf{min\text{-}B}}$ for the fundamental mode is 57°. Taking into account, however, the fact that there is a greater space of **k** values that are perpendicular to a vector than are parallel to a vector (area weighting of $\sin(\theta_{\mathbf{k\text{-}B}})$ in spherical coordinates), the average $\theta_{\mathbf{k\text{-}B}}$ for a random direction is also 57°. These results suggest that minimum variance analysis is not sufficient to determine the wave vector direction.

[14] The parallel compressibility C_B, on the other hand appears to be more nearly steady at a low value. The average value of C_B with the average weighted by the logarithm of the wave power is 0.27, indicating that the parallel magnetic fluctuations have about half the amplitude of the perpendicular fluctuations. The largest electric field component E_y ~ 1 mV/m and the largest magnetic component B_x ~ 0.3 nT, yielding $E_y/(c\ B_x) \sim 10^{-3}$. Thus these waves are predominantly electromagnetic.

[15] From Figure 1a, it appears that the wave power in the second harmonic at about 1 Hz is just as strong as the wave power at the fundamental frequency, at about 0.5 Hz. This is illusory because of the whitening of the spectra described earlier. Figure 3 shows the log average wave power versus frequency with no whitening and with a larger time window of about 20 s in order to increase the frequency resolution (~1/(20 s)). The fundamental mode (marked 1 in Figure 3) occurs at 0.485 Hz, and the higher harmonics (marked 2–4) are at higher frequency. This plot shows that the dominant wave power is in the fundamental mode, with about a factor of 3 greater power than that observed for the second harmonic.

3. Observed Distribution Functions

[16] The average pitch angle distribution of the electrons measured by the Cluster 1 (C1) PEACE instrument [*Johnstone et al.*, 1997] is shown in Figure 4 for 9 September 2003 from 0112 to 0115 UT (same time interval as for the waves). (We showed wave data from C3. There is very little difference between the plasma environments sampled by the different Cluster spacecraft for this segment of data, and the wave spectra observed by the different spacecraft are almost identical.) Very low energies are discarded because of photoelectron contamination. Figure 4 shows that the electron distribution is fairly isotropic ($T_{\|} \sim T_{\perp}$), and that the distribution function decreases for the most part monotonically with respect to particle velocity v. This makes it unlikely that the electron population is a source of instability.

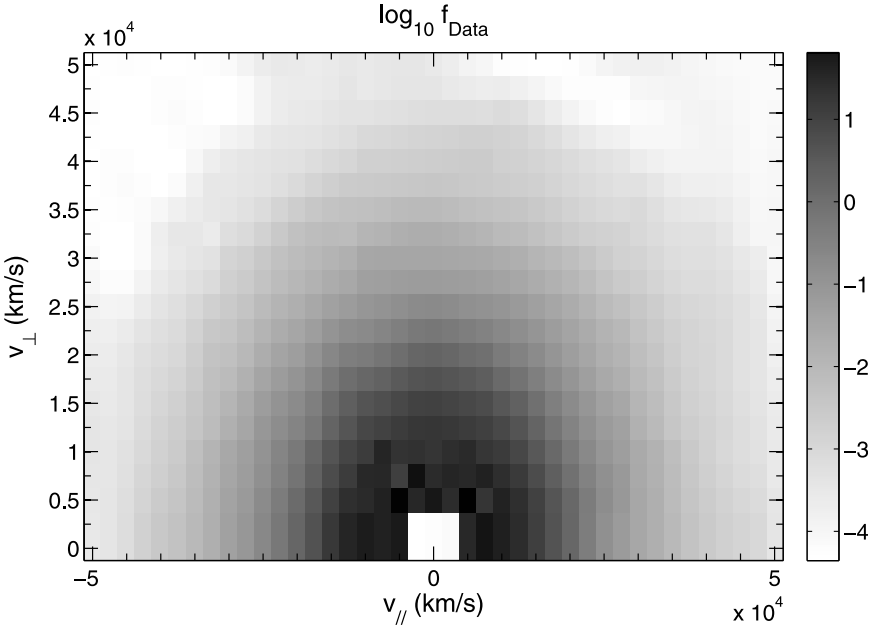

Figure 4. Average electron distribution function in s^3/km^6 in gray scale versus $v_{\|}$ on the horizontal axis and $v_{\perp}$ on the vertical axis, both measured in km/s.

Table 1. Model Electron Distribution Function

Component	n (cm^{-3})	$v_{th\parallel}$ (km/s)	$v_{th\perp}$ (km/s)	$T_\parallel$ (keV)	$T_\perp/T_\parallel$	$v_{0\parallel}$ (km/s)
1	0.498	10100.	9940.	0.292	0.963	9.0
2	0.00908	18800.	18500.	1.01	0.966	−0.1

[17] A model electron distribution composed of bi-Maxwellian components was determined by a semiautomatic procedure that minimized the difference between the model and observed distribution function. The exact procedure will be described elsewhere, but for now, we simply note that an error function is defined to represent the difference between the observed and model distribution function, and that the value of the error function is minimized to obtain an optimal fit. The observed distribution function was well fit by a two bi-Maxwellian electron components. Table 1 lists for these two components the density n, the parallel and perpendicular thermal velocities defined as $\sqrt{2T/m}$ (where T is the appropriate temperature), the parallel temperature $T_\parallel$, the temperature ratio $T_\perp/T_\parallel$, and the parallel drift velocity $v_{0\parallel}$.

[18] The good statistics for the electrons made it possible to get a good measure of the total electron density. The total electron density is 0.49 cm^{-3} using the observed distribution (interpolated into a rectangular grid) and 0.51 cm^{-3} for the model (superposition of two bi-Maxwellians). (At the beginning of the research described in this study, plasma wave data from the WHISPER instrument [*Décréau et al.*, 1997] was examined, and we thought that it suggested a plasma frequency ~6.5 kHz that was consistent with the above electron density ~0.5 cm^{-3}. After the research was finished, the WHISPER data was reexamined and it was decided that a plasma frequency of ~8–10 kHz was more consistent with the data. This would suggest an electron density up to a factor of 2 larger than that used in this study. Seeing as we have examined a large range of the effective ion beta (based on a best fit for the observed distribution function using a single Maxwellian distribution), β', in section 5, we do not think that it is necessary to redo our calculations, but this difference should be kept in mind. It could mean that the particle measurements should be scaled up, or that there is a very cold component of density that was not measured.)

[19] The Cluster Ion Spectroscopy instrument (CIS) [*Rème et al.*, 2001] has two components, the Hot Ion Analyzer (HIA) and the Composition Distribution Function (CODIF) instrument. Figure 5 shows the ion distribution function measured by the C1 HIA instrument for 9 September 2003 from 0112 to 0115 UT (same time interval as for the waves and electron data). The color bar on the right side of the plot shows the base 10 logarithm of the distribution function f_{Data} in units of s^3/km^6. Note that the entire scale is tinted in color. The white regions on the plot correspond to regions of velocity space for which there is not enough data to measure the distribution function. In particular, the central region around zero velocity is not measured. From Figure 5, we can see that there are two possible sources of instability, the dual beam-like feature composed of beams with parallel velocity equal to about ±500 km/s, and the shell or ring-like feature with smaller distribution function for smaller velocities of about 200–300 km/s than for larger velocities of about 600 km/s.

[20] Figure 6 shows Ion Model Distribution Function 1, which is composed of essentially five bi-Maxwellian components. This distribution function was found from the observed ion distribution function using a similar method to that used for the electron distribution function, that is, minimizing an error function. While this distribution function is not exactly like that in Figure 5, it does show the same general features of beam-like and ring-like distribution. The white lines in Figure 6 show the outer boundaries of the measured distribution function in Figure 5. Outside of these boundaries, we really don't know what the distribution function is.

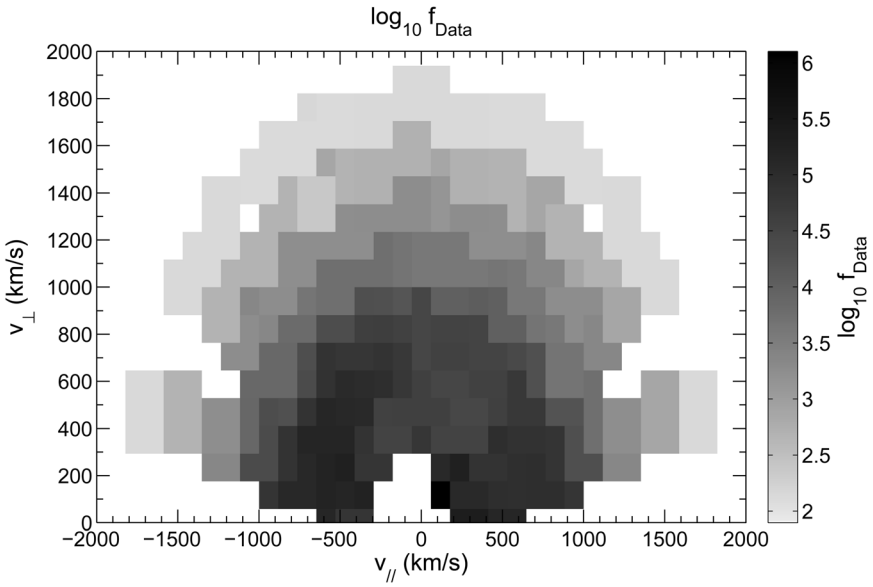

Figure 5. Average ion distribution function in s^3/km^6 in gray scale versus $v_\parallel$ on the horizontal axis and $v_\perp$ on the vertical axis, both measured in km/s.

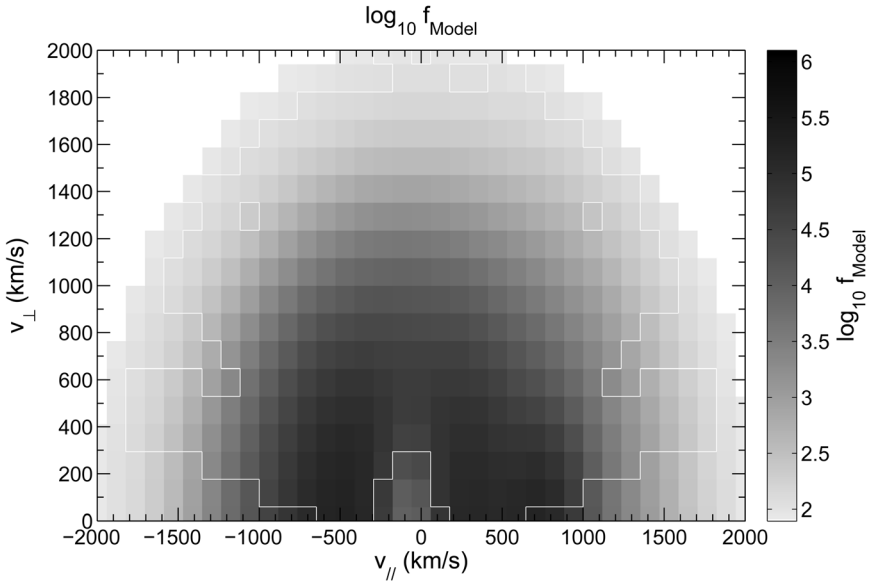

Figure 6. Model Ion Distribution Function 1 composed of essentially five bi-Maxwellian components in s^3/km^6 in gray scale versus $v_{||}$ on the horizontal axis and $v_\perp$ on the vertical axis, both measured in km/s. The white lines show the limits of the observed data from Figure 5.

[21] Table 2 shows the properties of the bi-Maxwellian components for Model Ion Distribution Function 1. Note carefully that the second component has negative density. By adding a low-temperature component with negative density, we are able to create the "ring-like" distribution function apparent in Figure 6. We said that there were essentially five components to the distribution. The sixth component listed in Table 2 is a low-density component that makes the distribution function greater than zero at several velocity space grid points in the inner region (low velocity) for which it would be negative otherwise (because of the negative density Component 2 in Table 2). This low-density component, however, does not alter the stability properties of the plasma at all based on our tests with and without it.

[22] The density of the ion components in Table 2 have been scaled up so that the total ion density is equal to that of the total model electron density in Table 1 (0.51 cm^{-3}). CIS CODIF results (not shown) showed a similar distribution function to HIA (but more noisy with some questionable features) and the total CODIF ion density was close to the 0.51 cm^{-3} value for the electrons. Also, from CODIF we did not see an appreciable density of O^+. Because of these facts, we decided to rescale the model distribution component densities determined from HIA so that the total ion density matched the total electron density of 0.51 cm^{-3}, assuming that all the ions were H^+. This procedure maximizes the possibility that the model distribution function will be unstable and helps to make up for the fact that our model distribution functions do not precisely capture the velocity space features of the observed ion distribution function (Figure 5).

[23] Figure 7 shows Model Ion Distribution Function 2, which has the seven components listed in Table 3. As we did for Model Ion Distribution Function 1, we rescaled the ion components so that the total density was 0.51 cm^{-3}, matching the electron density. Again there are negative density components which help to give a ring-like distribution function (low distribution function for ($v_{||}$, $v_\perp$) at about (0, 400) km/s). In Model 2, however, the distribution function is large for the very low velocities near the origin. (Model 2 did not have any velocities for which the distribution function was negative, so did not require any adjustment with an extra ion component.) While overall, Model 2 with its 7 components fits the observed data slightly better than Model 1, the difference in the fit is not great, and the greatest difference between the two models is in the region at very low velocities for which the ion distribution function is not observed (region outside white lines in Figures 6 and 7). For this reason, we do not necessarily consider Model 2 to be better than Model 1. And it's indeed possible that the actual distribution function could be something between the two.

4. Analysis of Instability

[24] Using the model distribution functions, either Model Ion Distribution Function 1 (Table 2), or Model Ion Distribution Function 2 (Table 3) with the model electron distribution function Table 1), we investigated the waves near harmonics of the ion cyclotron frequency and with wave vector $\boldsymbol{k}$ close to 90° from the background magnetic field (based on results by *Broughton et al.* [2008]) to look for instability using jWhamp, Dartmouth College's version of

Table 2. Model Ion Distribution Function 1

Component	n (cm^{-3})	$v_{th||}$ (km/s)	$v_{th\perp}$ (km/s)	$T_{||}$ (keV)	$T_\perp/T_{||}$	$v_{0||}$ (km/s)
1	0.756	503.	550.	1.32	1.20	−141.
2	−0.346	308.	465.	0.495	2.28	−100.
3	0.0476	515.	659.	1.382	1.64	504.
4	0.0268	194.	318.	0.197	2.68	737.
5	0.0209	1510.	1520.	11.8	1.02	0.185
6	0.00117	100.	200.	0.0522	4.00	−93.

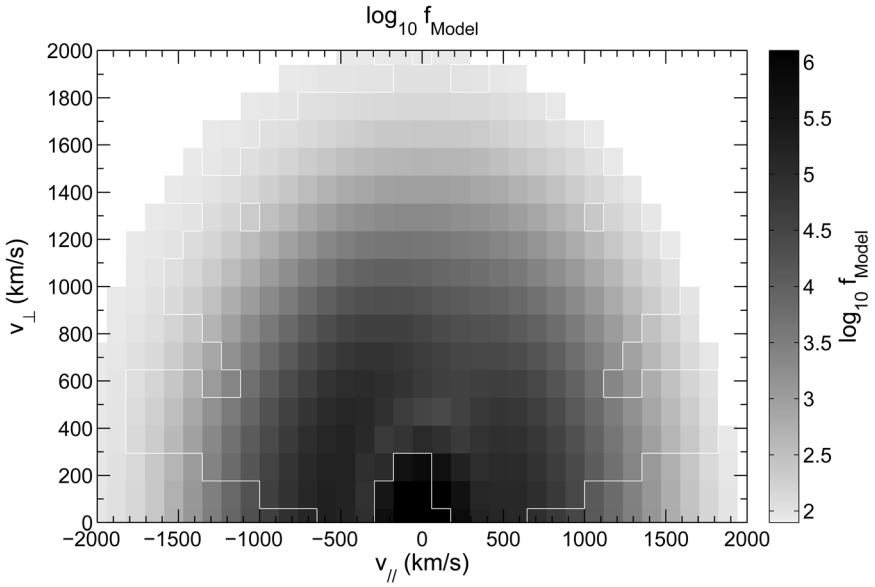

Figure 7. Same as Figure 6, but for Model Ion Distribution Function 2.

the well known electromagnetic plasma wave dispersion code WHAMP [*Rönnmark*, 1982, 1983].

[25] We did not find any instability using Model Ion Distribution Function 2. This distribution function, however, does not fully capture the details of the measured distribution function (Figure 5), and even if it did, it represents an average over several minutes that might not be characteristic of the distribution function during the time that the waves were generated. Because of this, we lowered the amplitude of the magnetic field by a factor of about 4, thereby increasing the plasma beta by a factor of 16, thinking that this might increase instability related to the velocity space features of the distribution function; but we still did not find any instability.

[26] With Model Ion Distribution Function 1, however, we did find an instability near the fundamental proton cyclotron frequency ($\omega = \Omega_{cp}$). The surface in Figure 8 shows the real frequency normalized to the proton gyrofrequency Ω_{cp} (vertical scale) versus $k_{\|}\rho_{\|}$ and $k_{\perp}\rho_{\|}$ (horizontal scales), with the normalized growth rate γ/Ω_{cp} indicated by color using the color bar at the right. Basically, red color corresponds to positive growth rate (instability), blue color corresponds to damping, and white corresponds to zero growth rate. The instability occurs around the border of a dip in the real frequency and close to the region where the real frequency increases. Figure 9 presents the same data in the form of a two dimensional contour plot for real frequency with the color again indicating the growth rate.

[27] For this event (9 September 2003, 0112–0115 UT), the amplitude of the background magnetic field is 32.8 nT, so the proton gyrofrequency $f_{cp} = \Omega_{cp}/(2\pi) = 0.498$ Hz ($\Omega_{cp} = 3.13$ s^{-1}), and $\rho_{\|} = v_{th\|}/\Omega_{cp} = 160$ km using $v_{th\|}$ for the first component in Table 2. The maximum growth rate $\gamma/\Omega_{cp} = 0.0289 \rightarrow \gamma = 0.0904$ s^{-1} occurs for $k_{\perp}\rho_{\|} = 3.16$ and $k_{\|}\rho_{\|} = 0.159 \rightarrow k_{\perp} = 0.0198$ km^{-1} and $k_{\|} = 0.000994$ km^{-1}, corresponding to a perpendicular wavelength of 317. km (about 1/20 R_E) and a parallel wavelength of 6320. km (about 1 R_E).

[28] Table 4 shows a comparison of the observed and theoretical wave properties. The normalized frequency ω/Ω_{cp} is close to unity in both cases (fundamental mode). The small value of $(\delta E)^2/(c\,\delta B)^2$ for both observed and theoretical waves ($\sim 10^{-3}$ and 0.0000747, respectively) indicates that the waves

Table 3. Model Ion Distribution Function 2

Component	n (cm^{-3})	$v_{th\|}$ (km/s)	$v_{th\perp}$ (km/s)	$T_{\|}$ (keV)	$T_{\perp}/T_{\|}$	$v_{0\|}$ (km/s)
1	0.733	503.	480.	1.32	0.908	−41.6
2	0.0224	2710.	3020.	38.4	1.24	−372.
3	0.160	666.	665.	2.32	0.996	35.7
4	−0.366	305.	360.	0.485	1.40	−129.
5	0.0234	184.	512.	0.177	7.73	−421.
6	−0.304	317.	473.	0.524	2.23	143.
7	0.237	199.	215.	0.207	1.16	−7.39

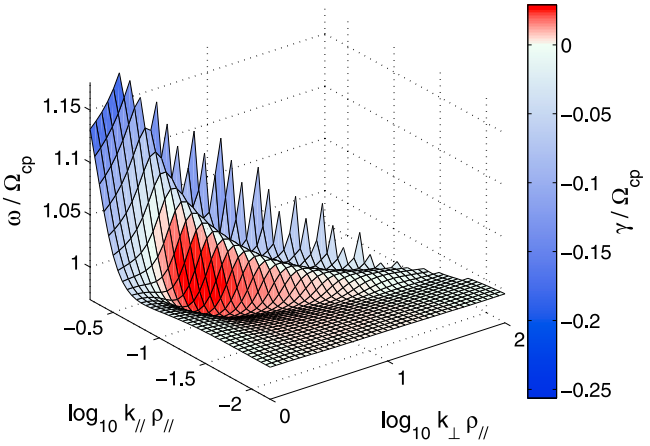

Figure 8. Surface showing the normalized real frequency ω/Ω_{cp} (vertical level) versus $k_{\|}\rho_{\|}$ and $k_{\perp}\rho_{\|}$ (horizontal scales), with the normalized growth rate γ/Ω_{cp} indicated by the color using the color bar at right.

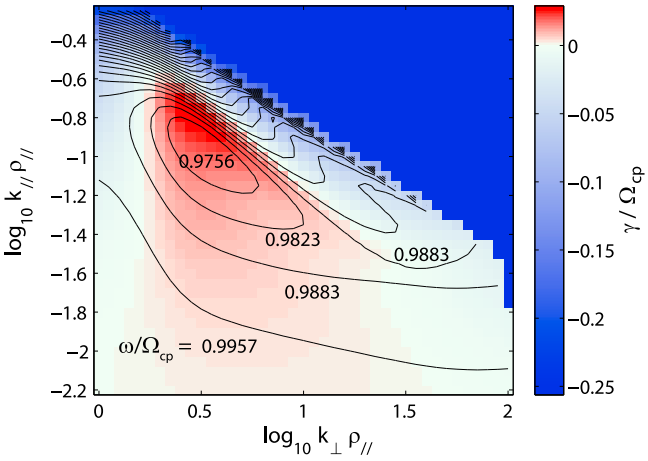

Figure 9. Contours of normalized real frequency ω/Ω_{cp} versus $k_{||}\rho_{||}$ and $k_{\perp}\rho_{||}$ with the normalized growth rate γ/Ω_{cp} indicated by the color using the color bar at right.

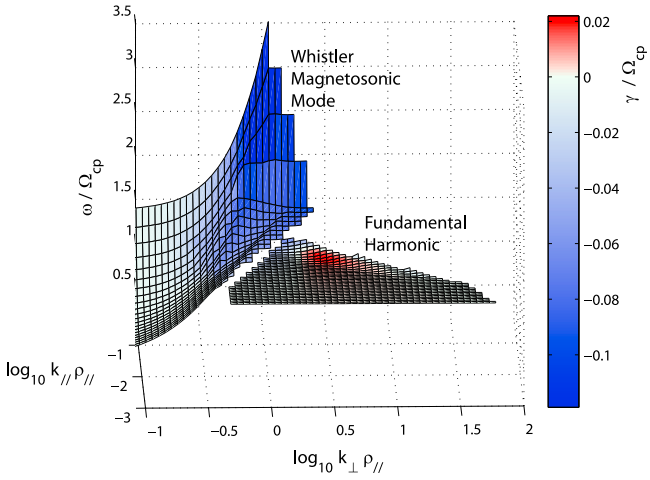

Figure 10. Surface plot for Model Ion Distribution Function 1, showing the normalized real frequency ω/Ω_{cp} versus $k_{||}\rho_{||}$ and $k_{\perp}\rho_{||}$ for the fundamental harmonic (primary mode studied in this paper) and the whistler/magnetosonic mode, with the normalized growth rate γ/Ω_{cp} indicated by the color using the color bar at right.

are predominantly electromagnetic (dominant magnetic component). The squared ratio of the electric field component in the $k_{\perp}$ direction relative to the total electric field component, $(\delta E_{k\perp})^2/(\delta E)^2$, is close to unity for the theoretical waves. Correspondingly (based on Faraday's law), the wave magnetic field major axis angle away from the $k_{\perp}$ direction, $\varphi_{maj\text{-}k\perp}$, is nearly equal to 90°. Since we don't know the $k_{\perp}$ direction, we don't have any corresponding information for the observed waves for these last two quantities. (The Cluster spacecraft were not in a favorable orientation to determine the wave vector for this event. If there is a superposition of waves, these quantities might not be well defined for the observed waves anyway.) The squared ratio of the parallel component of the wave magnetic field to the total component is 0.27 for the observed waves, and 0.182 for the theoretical waves. The ellipticity ε, argued to be close to zero in section 2, is also small for the theoretical wave, 0.0234. For Ion Distribution Function 1, the unstable surface with $\omega \cong \Omega_{cp}$ approaches the whistler/magnetosonic mode surface (Surface E of Figure 4 of *André* [1985]), but both waves are heavily damped where they approach each other (Figure 10).

[29] The WHAMP code also shows that the second and higher harmonics (ω/Ω_{cp} = 2, 3, …) are unstable. These will be examined further in a later manuscript, but for now we note that the fundamental mode had the largest growth rate (consistent with the fact that the fundamental mode had the largest observed wave power, as can be seen from Figure 3), and that the growth rate of the harmonics gradually decreases for the higher harmonics. By the 10th harmonic, the growth rate is reduced by a factor of three from that of the fundamental mode. (We did not test how many harmonics were unstable; we only checked up to ω/Ω_{cp} = 10.)

Table 4. Comparison of Observed and Theoretical Wave Properties

Property	Observed Waves	Theoretical Waves
ω/Ω_{cp}	~1 (Figure 3)	0.987
$(\delta E)^2/(c\ \delta B)^2$	$\sim 10^{-3}$	0.0000747
$(\delta E_{k\perp})^2/(\delta E)^2$	?	0.999
$C_B = (\delta B_{||})^2/(\delta B)^2$	0.27	0.182
Ellipticity ε	~0? (see discussion in section 2)	0.0234
B major axis angle $\phi_{maj\text{-}k\perp}$	?	89.8°

[30] In an effort to test the mechanism for the instability, we tested the stability of two model distribution functions with either beam-like or ring-like features. Figure 11 shows our beam-like ion distribution function with the parameters listed in Table 5. Again, the density of the components has been adjusted so that the total ion density is equal to the total electron density of 0.51 cm^{-3}. (The first component with very low density was included only to provide a normalization similar to that of the previous cases; WHAMP normalizes the wave vector using the thermal speed of the first species.) We did not find any instabilities with this distribution function.

[31] Figure 12 shows our ring-like distribution function with the parameters given in Table 6. Note that the negative density component has smaller temperature so that the distribution function is smaller for smaller velocities. In this case, there was an instability similar to that for Model Ion Distribution Function 1, as shown in Figure 13 (compare to Figure 9). The distribution function components have moderate temperature anisotropy ($T_{\perp}/T_{||}$ = 1.44 in Table 5) to better match the observed distribution function (Figure 5). The instability persists even if $T_{\perp}/T_{||}$ is reduced to unity for each component, showing that the instability is not driven by the temperature anisotropy, but by the ring-like distribution. Note that equatorial magnetosonic waves [*Meredith et al.*, 2008] at harmonics of Ω_{cp} are also thought to be driven by a ring-like distribution function. But those waves are predominantly compressional ($C_B = (\delta B_{||})^2/(\delta B)^2$ close to unity).

5. Dependence With Respect to the Effective Ion Beta β'

[32] We can investigate the dependence of the instability on the plasma beta by changing the amplitude of the mag-

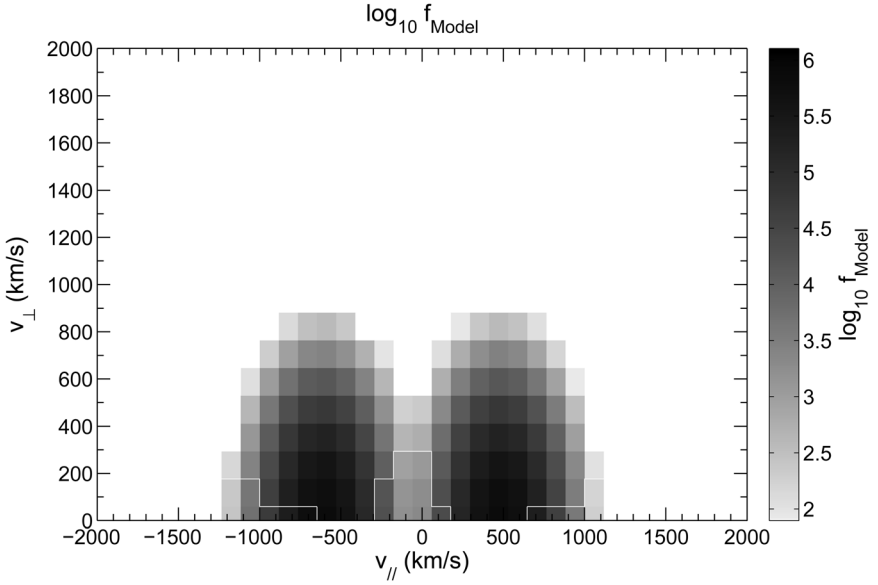

Figure 11. Beam-like distribution function tested for instability.

netic field. Table 7 shows properties of the instability (fundamental mode) using Model Ion Distribution Function 1 (Table 2) with a variation in the electron gyrofrequency, $F_{ce} = \Omega_{ce}/(2\pi)$ ($\propto B$), of a factor of 4000, resulting in a variation in the plasma beta ($\propto B^{-2}$) of a factor of 1.7×10^4. We are not suggesting here that the range of parameters listed will actually be observed in the magnetosphere; rather we are using a variation of the magnetic field to explore how the instability changes with respect to beta keeping the distribution function constant. The rows of Table 7 are arranged with the smallest values of F_{ce} (highest values of beta) at the top. The case of the original instability using the measured value of B (32.8 nT) is shown with $F_{ce} = 0.918$ kHz and marked with the notation "original case." The instability is quite robust, as it persists over the entire range of beta.

[33] While it's difficult to precisely define beta for the multicomponent population represented by Model Ion Distribution 1, we can define an approximate single component ion beta, β'. For this, we fit the entire ion distribution function with a single bi-Maxwellian, and scale up the proton density to the electron value (as discussed in section 3) to get $n_p = 0.51$, $T_{\|p} = 2.3$ keV, and $T_{\perp p} = 2.0$ keV. Taking an average temperature $T_p = 2\ T_{\perp p}/3 + T_{\|p}/3 = 2.1$ keV, we get $\beta' = 8\pi n_p T_p/B^2 = 0.40$ for the original case. Then the values of β' in Table 7 for other F_{ce} scale like F_{ce}^{-2}.

[34] The properties of the instability change as a function of β'. Note that $(\delta E_k)^2/(\delta E)^2$ is close to unity for the whole range of parameters, showing that the electric field is electrostatic in this sense. If this quantity were exactly equal to unity, the wave would be totally electrostatic (purely electric), since when $\delta \boldsymbol{E}$ is exactly parallel to the wave vector k, $\delta \boldsymbol{B} = 0$ by Faraday's law. But Table 7 shows that the magnetic energy is dominant for β' greater than about 5×10^{-4}. (Note that $(\delta E)^2/(c\ \delta B)^2$ is the ratio of electric to magnetic energy in the wave.) For very small β', $(\delta E)^2/(c\ \delta B)^2$ becomes very large (331 for $\beta' = 2.1 \times 10^{-5}$). For the original case ($\beta' = 0.40$), $(\delta E)^2/(c\ \delta B)^2 = 7.5 \times 10^{-5}$ showing that the wave is strongly electromagnetic. While the perpendicular components of the perturbed magnetic field $\delta \boldsymbol{B}$ are larger than the parallel component ($C_B = (\delta B_{\|})^2/(\delta B)^2 = 0.182$), the parallel component is significant (43% of the total vector). As β' is increased to values greater than about 2, the instability becomes predominantly compressional ($C_B = (\delta B_{\|})^2/(\delta B)^2 > 0.5$).

[35] As F_{ce} is increased from a value ~1 to 128 kHz, the normalized growth rate γ/Ω_{cp} decreases, but because Ω_{cp} is increasing, the unnormalized (absolute) growth rate γ actually increases. This is especially the case for F_{ce} between 16 and 64 kHz, for which the normalized growth rate is almost constant. Note that this is where there is a transition from an electromagnetic wave to an electrostatic wave at about $F_{ce} =$ 32 kHz. Apparently the instability is stronger if it can be electrostatic, which occurs at smaller plasma β' than the "original case" that we analyzed. That is, lower β' is actually preferred for this instability. As F_{ce} is increased above 128 kHz (not shown in Table 4), the unnormalized growth rate does eventually decrease (eventually like $\gamma \propto F_{ce}^{-1} \propto B^{-1}$), but for this large F_{ce},. the Alfven speed is approaching the speed of light. The peak growth rate occurs for F_{ce} between 128 and 256 kHz, corresponding to β' of about 1×10^{-5}. As F_{ce} is decreased from the original case (increasing β'), the normalized growth rate γ/Ω_{cp} decreases, indicating a strong decrease in the unnormalized growth rate (especially from $F_{ce} = 0.5$ to 0.25 kHz, for which γ/Ω_{cp} decreases from 0.0187 to 0.0035, a factor of about 5, corresponding to a drop in γ of about 10). As F_{ce} is decreased further from 0.125 to 0.03125 kHz, the normalized growth rate γ/Ω_{cp} becomes nearly constant indicating that $\gamma \propto F_{ce} \propto B$ in this regime.

Table 5. Beam-Like Model Ion Distribution Function

Component	n (cm^{-3})	$v_{th\|\|}$ (km/s)	$v_{th\perp}$ (km/s)	$T_{\|\|}$ (keV)	$T_\perp/T_{\|\|}$	$v_{0\|\|}$ (km/s)
1	0.000426	600.	600.	1.88	1.00	−65.0
2	0.249	200.	300.	0.209	2.25	−615.
3	0.249	200.	300.	0.209	2.25	485.

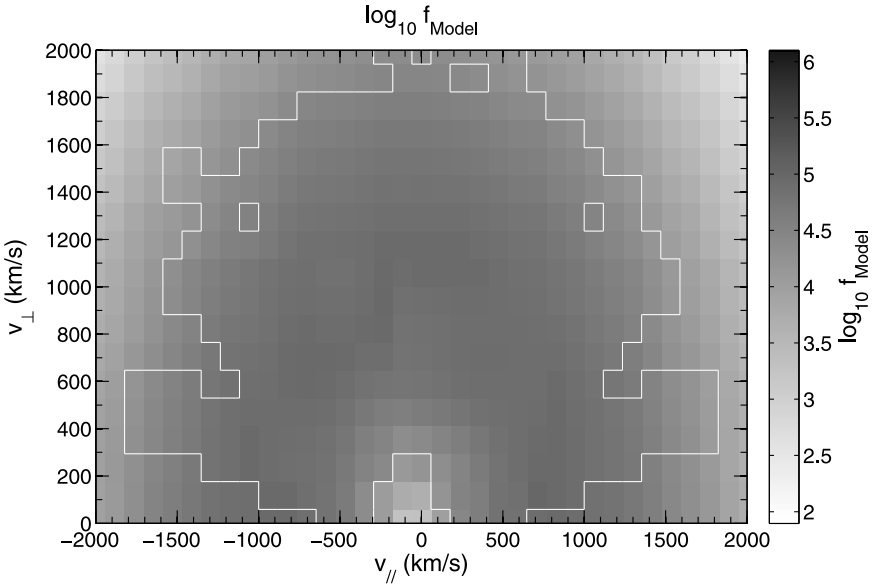

Figure 12. Model ring-like ion distribution function.

[36] On the other hand, if we regard our variation of F_{ce} simply as a convenient device to vary the plasma beta, and consider the case of constant magnetic field amplitude B (or constant F_{ce}) with varying plasma pressure, then Table 7 shows that the maximum growth rate occurs at the maximum value of γ/Ω_{cp}, at β' equal to 0.4, which is close to the observed parameters. In other words, the waves were observed when the plasma conditions were nearly ideal for the instability.

6. Discussion

[37] Several studies have pointed out that as spacecraft move from the PSBL to the CPS the ion distributions change from two crescent-shaped distributions in velocity space, to a ring-shaped distribution, and ultimately to the hot ions of the CPS. Wave activity has often been suggested as the agent responsible for part or all of this transition [e.g., *Gary and Winske*, 1990] (and others reviewed by *Broughton et al.* [2008]), and the harmonic waves reported here show a very close observational link to the PSBL, and, in particular, to its ring-shaped particle distributions. These waves may thus play an important role in energizing the plasma sheet.

[38] Both electron and ion beams have been suggested as the source of these waves, and both are observed during each of these wave events. *Broughton et al.* [2008] reviewed many earlier studies investigating possible instabilities that might drive them, and suggested that the two most likely sources of these multiple-harmonic waves were (1) inverse Landau resonance with an accelerated electron beam as described by *Chaston et al.* [2002], or (2) the electromagnetic ion/ion instability caused by coupling between a slow wave on the ion beam and the background ions, as described by *Winske and Omidi* [1992].

[39] *Broughton et al.* [2008] compared the occurrence of waves only with properties of suprathermal ions, whereas in this study and in the companion study by *Engebretson et al.* [2010] we have included electron distributions as well. Although there was a strong correlation between the occurrence of harmonic waves and streaming populations of both energetic ions and energetic electrons, *Engebretson et al.* [2010] noted that the correlation was stronger with increased fluxes of energetic ions, and in every case the ion beta exceeded the electron beta by a factor of ~9.

[40] Contrary to the assumptions of the study of *Gary and Winske* [1990], the beam-like portions of the observed distributions modeled in this study did not generate electromagnetic instability. Because other wave modes have also

Table 6. Ring-Like Model Ion Distribution Function

Component	n (cm^{-3})	$v_{th\|\|}$ (km/s)	$v_{th\perp}$ (km/s)	$T_{\|\|}$ (keV)	$T_\perp/T_{\|\|}$	$v_{0\|\|}$ (km/s)
1	0.0000324	600.	600.	1.88	1.00	−65.0
2	3.15	900.	1080.	4.23	1.44	−65.0
3	−2.65	850.	1020.	3.77	1.44	−65.0

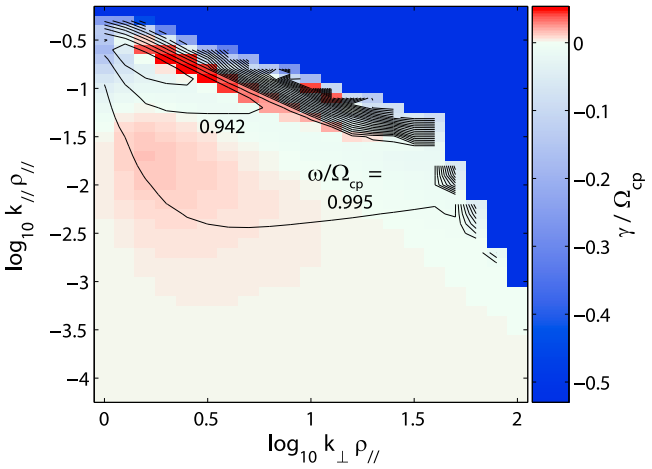

Figure 13. Same as Figure 9, but for the ring-like ion distribution function.

Table 7. Instability Properties as a Function of Electron Gyrofrequency

F_{ce} (kHz)	β'	$\log_{10}(k_\perp \rho_\parallel)$	$\log_{10}(k_\parallel \rho_\parallel)$	ω/Ω_{cp}	γ/Ω_{cp}	$(\delta E_k)^2/(\delta E)^2$	$(\delta E)^2/(c\ \delta B)^2$	$C_B = (\delta B_\parallel)^2/(\delta B)^2$
0.03125	3.4×10^{2}	0.40	−1.55	0.994	0.0030		1.7×10^{-5}	0.996
0.0625	8.6×10^{1}	0.40	−1.55	0.994	0.0030	0.974		0.996
0.125	2.2×10^{1}	0.40	−1.55	0.994	0.0031			
0.25	5.4	0.45	−1.45	0.990	0.0035	0.981		0.993
0.5	1.3	0.50	−0.45	0.972	0.0187	0.978		0.317
0.918 (original case)	0.40	0.45	−0.80	0.98	0.0220	0.9954	7.5×10^{-5}	0.182
1	0.34	0.45	−0.80	0.991	0.0211			
2	8.4×10^{-2}	0.45	−1.10	0.993	0.0122	0.9991	3.7×10^{-4}	0.0534
4	2.1×10^{-2}	0.45	−1.35	0.994	0.0071			
8	5.3×10^{-3}	0.50	−1.55	0.9955	0.0049	0.99998	1.4×10^{-2}	
16	1.3×10^{-3}	0.50	−1.60	0.9961	0.0043		0.121	
32	3.3×10^{-4}	0.50	−1.65	0.9959	0.0042	0.99999999	2.21	
64	8.2×10^{-5}	0.50	−1.65	0.9953	0.0040			
128	2.1×10^{-5}	0.45	−1.65	0.9941	0.0035	~1.	331.	0.002

been observed in the PSBL, including electrostatic waves with frequencies near or above the lower hybrid frequency and more broadband electrostatic and electromagnetic waves above Ω_{cp}, it is possible that the transition from ion beams to ring distributions to isotropic distributions occurs in stages, mediated by two or more kinds of waves. Or the ring distributions could result from beam-like distributions that have evolved due to simple propagation effects [*Onsager et al.*, 1991]. In any case, some other effect must be responsible for the transition from beam to ring distributions, but the ion ring distribution stage may well be responsible for the fundamental electromagnetic waves mode near Ω_{cp}, and hence may play a key role in the final transition to the isotropic plasma distributions of the central plasma sheet.

[41] As shown in section 2, we were not able to get a reliable estimate of the angle between the minimum variance direction and the background magnetic field, $\theta_{\text{min-}\mathbf{B}}$, from which the wave normal angle $\theta_{\mathbf{k\text{-}B}}$ might be inferred. The much more reliable method to determine the direction of the wave vector is the wave telescope technique used by *Broughton et al.* [2008]. Broughton *et al.* used this technique to analyze all the multiple harmonic electromagnetic wave events observed by Cluster between approximately 2002 and 2006 for which the Cluster spacecraft configuration was adequate to get reliable results (three events). For all of these events, the wave vector $\boldsymbol{k}$ was nearly perpendicular to the background field $\boldsymbol{B}$, suggesting that that is probably the case for our event as well.

[42] The instability is driven by a positive slope in the distribution function with respect to the perpendicular particle velocity $v_\perp$, as, for example, demonstrated by *Janhunen et al.* [2003]. The Maxwellian electrons do not contribute to wave growth, but rather damp the mode via Landau damping. Janhunen *et al.* considered only the low-beta plasmas of the auroral ionosphere, in which the instability propagates almost perpendicular to the background magnetic field. As beta increases toward magnetospheric values near unity, the propagation angle moves somewhat away from the perpendicular (Table 7), but the basic physics remains the same: the instability grows at frequencies which are multiples of the proton cyclotron frequency and, as suggested by the simulations of Janhunen *et al.*, is presumably stabilized by scattering of the ions in $v_\perp$, removing the ion free energy which drives the unstable mode.

[43] The variation in wave-like properties with respect to the effective ion beta β' examined in section 5 suggests that there might be a continuous transition between electrostatic waves at extremely low β' to perpendicularly polarized electromagnetic waves (such as we observed) at low β' to compressional electromagnetic waves at high β'. In fact, the plasma parameters of *Cattell and Hudson* [1982] (who observed electrostatic waves at harmonics of Ω_{cp}) correspond to $\beta' = 10^{-7}$, which is well below the limit we found for electrostatic waves. On the other hand, the parameters of *Boardsen et al.* [1992] (who observed compressional magnetosonic waves) correspond to β' about a factor of 10 lower than we found for our event. It is possible that the exact distribution function might make a difference in the exact beta boundaries. It is also likely that different distribution functions would excite different harmonics to differing degrees.

7. Conclusions

[44] Model ion velocity distributions composed of multiple bi-Maxwellian components were created to match the observed pitch angle distributions of ions and electrons in the midtail PSBL. These distributions included both beam-like and ring-like components, and were analyzed for wave instabilities using the WHAMP electromagnetic plasma wave dispersion code. A modeled distribution that included a core of cold plasma was found to be stable, whereas the model that did not include such a cold plasma component exhibited an instability near Ω_{cp}. Further instability analysis using simple model distributions with only beam-like or ring-like features suggested that the instability was driven by the ring-like feature (the relative absence of ions with energies below about 700 eV) rather than the simultaneously observed counterstreaming of the ion fluxes. If this conclusion is correct, then the consistent association between counterstreaming ion fluxes and wave events found in the survey of *Engebretson et al.* [2010] is not directly responsible for wave onset, but rather an artifact of the conditions associated with the PSBL. However, counterstreaming ion fluxes might still be a necessary part of the physical processes occurring in the PSBL, in two ways. First, the ion beams could be necessary to transport ions to the location at which they became unstable to local generation of the waves, and second, the beam-like distributions could evolve into ring like distributions, perhaps through the mediation of some other waves or propagation effects, as suggested above.

[45] Our analysis indicates that this instability persists over an enormous range in the effective ion beta β', but that

the character of the instability changes with β'. For β' of order unity (for instance, the observed case with $\beta' \sim 0.4$), the instability is predominantly electromagnetic; the fluctuating magnetic field has components in both the perpendicular and parallel directions, but the perpendicular fluctuations are larger. If β' is greatly decreased to about $5. \times 10^{-4}$ (by increasing the magnetic field), the instability becomes electrostatic. Near β' of order unity, the unnormalized growth rate of the instability actually increases as β' decreases. On the other hand, if β' is increased (by decreasing the magnetic field), the instability remains electromagnetic, but becomes predominantly compressional (magnetic fluctuations predominantly parallel) at $\beta' \sim 2$. If we consider the case of constant magnetic field, then the observed waves occurred at nearly the exact pressure for maximum growth rate (section 6). One must keep in mind that the results based on Ion Model Distribution 1 are an extreme case (nearly zero distribution function at low velocities). It is certainly possible that the real distribution leading to instability was something in between Model Ion Distribution Function 1 (Table 2) and Model Ion Distribution Function 2 (Table 3), and that the instability in the real PSBL had properties not quite as robust as those described above. We expect, however, that the general properties of the instability will be similar.

[46] As noted above, harmonic frequencies were also unstable but with decreasing growth rate with respect to harmonic number. Considering the fact that the theoretical waves have properties matching those of the observed waves (Table 4), the fact that the theoretical fundamental mode has the greatest growth rate and observed wave power, that harmonics are also unstable theoretically and observed, and that the theoretical instability has nearly the ideal pressure for the greatest growth rate, we feel fairly confident that our theoretical analysis gives an adequate description for the observed waves.

[47] **Acknowledgments.** We thank Barrett Rogers of Dartmouth College for helpful conversations, and Karl-Heinz Fornaçon of the Technical University of Braunschweig for assistance in obtaining the Cluster FGM data. Work at Dartmouth College was supported by NSF grants ANT-0538379 and ATM-0120950 (Center for Integrated Space Weather Modeling, CISM, funded by the NSF Science and Technology Centers Program). Work at Augsburg College was supported by NSF grants ATM-0827903 and ANT-0538379. Work at the University of California, Berkeley, was supported by NASA grant NNX08AF29G. Work at UCL-MSSL was supported by UK STFC Rolling grant PP/E/001173/1. The Los Alamos portion of this work was performed under the auspices of the U.S. Department of Energy, and was supported by the Defense Threat Reduction Agency under their "Basic Research for Combating Weapons of Mass Destruction" Program, IACRO 10–4946I. Work at the University of Minnesota was supported by NASA grants NNG04GG83G and NNX08AF28G. Cluster work at LPC2E and CESR was funded by CNES grants.

[48] Masaki Fujimoto thanks Peter Yoon and another reviewer for their assistance in evaluating this paper.

References

Anderson, B. J., R. E. Denton, and S. A. Fuselier (1996), On determining polarization characteristics of ion cyclotron wave magnetic field fluctuations, *J. Geophys. Res.*, *101*, 13,195.

André, M. (1985), Dispersion surfaces, *J. Plasma Phys.*, *33*(1), 1.

Angelopoulos, V., W. Baumjohann, C. F. Kennel, F. V. Coroniti, M. G. Kivelson, R. Pellat, R. J. Walker, H. Lühr, and G. Paschmann (1992), Bursty bulk flows in the inner central plasma sheet, *J. Geophys. Res.*, *97*, 4027–4039.

Angelopoulos, V., C. Kennel, F. Coroniti, R. Pellat, M. Kivelson, R. Walker, C. Russell, W. Baumjohann, W. Feldman, and J. Gosling (1994), Statistical characteristics of bursty bulk flow events, *J. Geophys. Res.*, *99*, 21,257–21,280.

Ashour-Abdalla, J., N. Leboeuf, D. Schriver, J.-M. Bosqued, N. Cornilleau-Wehrlin, V. Sotnikov, A. Marchaudon, and A. N. Fazakerley (2006), Instabilities driven by ion shell distributions observed by Cluster in the midaltitude plasma sheet boundary layer, *J. Geophys. Res.*, *111*, A10223, doi:10.1029/2005JA011490.

Balogh, A., et al. (2001), The Cluster magnetic field investigation: Overview of in-flight performance and initial results, *Ann. Geophys.*, *19*, 1207–1217.

Baumjohann, W., G. Paschmann, and H. Lühr (1990), Characteristics of high-speed ion flows in the plasma sheet, *J. Geophys. Res.*, *95*, 3801–3809.

Boardsen, S. A., D. L. Gallagher, D. A. Gurnett, W. K. Peterson, and J. L. Green (1992), Funnel-shaped, low-frequency equatorial waves, *J. Geophys. Res.*, *97*, 14,967–14,976.

Broughton, M. C., M. J. Engebretson, K.-H. Glassmeier, Y. Narita, A. Keiling, K.-H. Fornacon, G. K. Parks, and H. Rème (2008), Ultra-low-frequency waves and associated wave vectors observed in the plasma sheet boundary layer by Cluster, *J. Geophys. Res.*, *113*, A12217, doi:10.1029/2008JA013366.

Cattell, C., and M. Hudson (1982), Flute mode waves near ω_{LH} excited by ion rings in velocity space, *Geophys. Res. Lett.*, *9*(10), 1167–1170.

Chaston, C. C., J. W. Bonnell, J. P. McFadden, R. E. Ergun, and C. W. Carlson (2002), Electromagnetic ion cyclotron waves at proton cyclotron harmonics, *J. Geophys. Res.*, *107*(A11), 1351, doi:10.1029/2001JA900141.

Décréau, P. M. E., P. Fergeau, V. Krasnosel'skikh, M. Lévêque, P. Martin, O. Randriamboarison, F. X. Sené, J. G. Trotignon, P. Canu, and P. B. Mögensen (1997), WHISPER, a resonance sounder and wave analyser: Performances and perspectives for the CLUSTER misssion, *Space Sci. Rev.*, *79*, 157–193.

Denton, R. E., B. J. Anderson, G. Ho, and D. C. Hamilton (1996), Effects of wave superposition on the polarization of electromagnetic ion cyclotron waves, *J. Geophys. Res.*, *101*, 24,869.

Eastman, T. E., L. A. Frank, W. K. Peterson, and W. Lennartsson (1984), The plasma sheet boundary layer, *J. Geophys. Res.*, *89*, 1553–1572.

Eastman, T. E., L. A. Frank, and C. Y. Huang (1985), The boundary layers as the primary transport regions of the Earth's magnetotail, *J. Geophys. Res.*, *90*, 9541–9560.

Engebretson, M. J., W. K. Peterson, J. L. Posch, M. R. Klatt, B. J. Anderson, C. T. Russell, H. J. Singer, R. L. Arnoldy, and H. Fukunishi (2002), Observations of two types of Pc 1–2 pulsations in the outer dayside magnetosphere, *J. Geophys. Res.*, *107*(A12), 1451, doi:10.1029/2001JA000198.

Engebretson, M. J., C. R. G. Kahlstorf, J. L. Posch, A. Keiling, A. P. Walsh, R. E. Denton, M. C. Broughton, C. J. Owen, K.-H. Fornaçon, and H. Rème (2010), Multiple harmonic ULF waves in the plasma sheet boundary layer observed by Cluster, *J. Geophys. Res.*, *115*, A12225, doi:10.1029/2010JA015929.

Gary, S. P., and D. Winske (1990), Computer simulations of electromagnetic instabilities in the plasma sheet boundary layer, *J. Geophys. Res.*, *95*, 8085–8094, doi:10.1029/JA095iA06p08085.

Grabbe, C. L., and T. E. Eastman (1984), Generation of broadband electrostatic noise by ion beam instabilities in the magnetotail, *J. Geophys. Res.*, *89*, 3865–3872.

Grigorenko, E. E., J.-A. Sauvaud, and L. M. Zelenyi (2007), Spatial-temporal characteristics of ion beamlets in the plasma sheet boundary layer of magnetotail, *J. Geophys. Res.*, *112*, A05218, doi:10.1029/2006JA011986.

Horne, R. B., G. V. Wheeler, and H. S. K. Alleyne (2000), Proton and electron heating by radially propagating fast magnetosonic waves, *J. Geophys. Res.*, *105*, 27,597–27,610.

Janhunen, P., A. Olsson, A. Vaivads, and W. K. Peterson (2003), Generation of Bernstein waves by ion shell distributions in the auroral region, *Ann. Geophys.*, *21*, 881–891.

Johnstone, A. D., et al. (1997), Peace: A Plasma Electron and Current Experiment, *Space Sci. Rev.*, *79*, 351–398.

Kokubun, S., M. Takami, K. Hayashi, H. Fukunishi, I. Kimura, A. Sawada, and Y. Kasahara (1991), Triaxial search coil measurements of ELF waves in the plasmasphere: Initial results from EXOS-D, *Geophys. Res. Lett.*, *18*, 301–304.

Liu, H., S. Kokubun, and K. Hayashi (1994), Equatorial electromagnetic emission with discrete spectra near harmonics of oxygen gyrofrequency during magnetic storm, *Geophys. Res. Lett.*, *21*, 225–228.

Meredith, N. P., R. B. Horne, and R. R. Anderson (2008), Survey of magnetosonic waves and proton ring distributions in the Earth's inner magnetosphere, *J. Geophys. Res.*, *113*, A06213, doi:10.1029/2007JA012975.

Olsson, A., P. Janhunen, and W. K. Peterson (2004), Ion shell distributions as free energy source for plasma waves on auroral field lines mapping to plasma sheet boundary layer, *Ann. Geophys.*, *22*, 2115–2133.

Onsager, T. G., M. F. Thomsen, R. C. Elphic, and J. T. Gosling (1991), Model of electron and ion distributions in the plasma sheet boundary layer, *J. Geophys. Res.*, *96*, 20,999–21,011.

Parks, G. K., et al. (1984), Particle and field characteristics of the high-latitude plasma sheet boundary layer, *J. Geophys. Res.*, *89*, 8885–8906.

Perraut, S., A. Roux, P. Robert, R. Gendrin, J.-A. Sauvaud, J.-M. Bosqued, G. Kremser, and A. Korth (1982), A systematic study of ULF waves above F_H^+ from GEOS 1 and 2 measurements and their relationships with proton ring distributions, *J. Geophys. Res.*, *87*, 6219–6236.

Pokhotelov, O. A., D. O. Pokhotelov, F. Z. Feygin, V. A. Gladychev, M. Parrot, K. Hayashi, J. Kangas, and K. Mursula (1997), Oxygen cyclotron harmonic waves in the deep plasmasphere during magnetic storms, *J. Geophys. Res.*, *102*, 77–83.

Rème, H., et al. (2001), First multispacecraft ion measurements in and near the Earth's magnetosphere with the identical Cluster ion spectrometry (CIS) experiment, *Ann. Geophys.*, *19*, 1303–1354.

Rönnmark, K. (1982), WHAMP: Waves in homogeneous, anisotropic, multicomponent plasmas, *Rep. 179*, Kiruna Geophys. Inst., Kiruna, Sweden.

Rönnmark, K. (1983), Computation of the dielectric tensor of a Maxwellian plasma, *Plasma Phys.*, *25*, 699.

Russell, C. T., R. E. Holzer, and E. Smith (1970), OGO 3 observations of ELF noise, *J. Geophys. Res.*, *75*, 755–768.

Winske, D., and N. Omidi (1992), Electromagnetic ion/ion cyclotron instability: Theory and simulations, *J. Geophys. Res.*, *97*, 14,779, doi:10.1209/92JA00902.

C. A. Cattell, School of Physics and Astronomy, University of Minnesota, Minneapolis, MN 55455, USA. (cattell@fields.space.umn.edu)

P. M. E. Décréau, LPC2E, UMR 6115, CNRS, F-45071 Orléans CEDEX 2, France. (pierrette.decreau@cnrs-orleans.fr)

R. E. Denton, Department of Physics and Astronomy, Dartmouth College, Hanover, NH 03755, USA. (richard.e.denton@dartmouth.edu)

M. J. Engebretson, Department of Physics, Augsburg College, 2211 Riverside Ave., Minneapolis, MN 55454, USA. (engebret@augsburg.edu)

S. P. Gary, Group ISR-1, Los Alamos National Laboratory, M.S. D466, Los Alamos, NM 87545, USA. (pgary@lanl.gov)

A. Keiling, Space Sciences Laboratory, University of California, Berkeley, CA 94720, USA. (keiling@ssl.berkeley.edu)

H. Rème, CESR, University of Toulouse, UPS, 9 ave. du Colonel Roche, F-31028 Toulouse CEDEX 4, France. (reme@cesr.fr)

A. P. Walsh, Mullard Space Science Laboratory, University College London, Holmbury St. Mary, Dorking RH5 6NT, UK. (apw@mssl.ucl.ac.uk)